Microstructure and Property Optimization of LENS Deposited H13 Tool Steel

J. Brooks[†], C. Robino[‡], T. Headley[‡], S. Goods[†], M. Griffith[‡]

Sandia National Laboratories
[†]Livermore, CA and [‡]Albuquerque, NM

Introduction

Direct laser metal deposition is a means of near net shape processing that offers a number of advantages including rapid prototyping and small lot production. With the LENS (Laser Engineered Net Shape) process [Ref 1], parts are fabricated by creating a laser melted pool into which particles are injected. Fabrication proceeds by moving the work piece, thereby building the structure line by line and layer by layer. In this manner a wide variety of geometries and structures can be fabricated. During fabrication, a complex thermal history is experienced in different regions of the build. These thermal histories include remelting and numerous lower temperature thermal cycles. Furthermore, the use of a finely focused laser to form the rapidly traversing pool can result in relatively high solidification velocities and cooling rates.

Previous work has developed LENS as an advanced manufacturing tool rather than exploiting its potentially unique attributes: real time control of microstructure, tailored material properties at different part locations, the production of graded structures, etc. Very often, however, material properties are not significantly different than those of wrought materials.

The goal of this program is to exploit the unusual thermal environment experienced during fabrication, and the ability to design and vary alloy composition. In this paper we describe this approach using H13 tool steel in which only the thermal fields are varied through changing process parameters to achieve desired properties.

Approach Our desire in this program is to demonstrate the ability to "process for properties" which is necessary to fully utilize the unique attributes of this process. The approach requires at least four basic steps: (1) Select or design an alloy system with the metallurgical characteristics capable of producing the required engineering properties. (2) Develop and experimentally validate process models that can be used to describe the thermal history for different processing parameters in any region, or at least critical regions of the build. (3) Develop a material model which describes the relevant microstructural changes and properties during processing. (4) Combine the process and microstructural models to predict and tailor build properties.

In this paper we have used H-13 tool steel to demonstrate this approach. This is a commercially available secondary hardening alloy that is of significant industrial importance and which exhibits a martensitic structure tempered with the formation of alloy carbides. The alloy composition is shown in Table 1.

Table 1.
Composition of H13 (wt%)

C	Mn	Si	Cr	Mo	V	P	S	Fe
0.38	0.35	1.0	5.52	1.61	0.87	.009	0.18	Bal.

Process Thermal Model Microstructural interpretations and predictions require precise knowledge of the thermal history. In this study single line widths were used to fabricate thin wall square shells 6.35 cm on a side. Single line wall builds 5.1 cm long were also fabricated. A

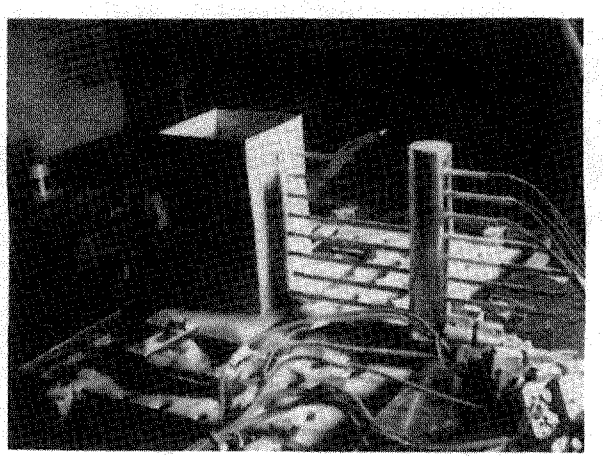

(a)

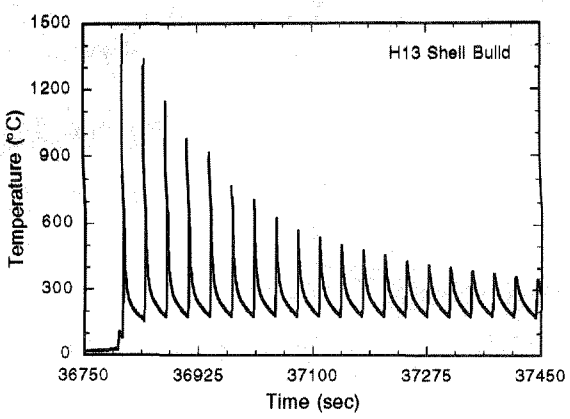

(b)

Figure 1 (a) Experimental setup for thermocouple measurements of single line width shell builds. (b) Results from one of the thermocouples shown in (a).

range of travel speeds of 5.9, 7.7, 9.3 mm/s using continuous YAG laser powers of 200, 250 and 300 watts produced individual layer thicknesses of ~ 0.25 mm with widths of ~ 0.4 mm. Temperature measurements were made using the experimental setup shown in Figure 1(a). Thermocouples 0.13 mm in diameter were inserted into parts during the build, and data was collected at 100 Hz.

Results from one of the thermocouples are shown in Figure 1(b). The first thermal cycle depicts the cooling from the molten pool. The subsequent thermal cycles, occurring every 33 seconds as the next layer is deposited, correspond to the thermal exposure of the underlying passes. Results are shown for 20 cycles, or build passes, where it can be seen that peak temperatures decrease in each succeeding pass. In the first pass the maximum cooling rate is ~$5x10^3$°C/sec. With these shell builds little heat is built-up with the interpass temperature remaining at ~150°C. Thermal predictions have been made using simple Rosenthal analytical solutions [Ref 2] as well as with FEM using element birthing techniques. However, as has been demonstrated for weld process models [Refs 3,4], experimental data such as that shown in Figure 1(b) is critical for model validation. In this study the experimental data, rather than a thermal model, was used for microstructural predictions. However, we must point out that for true "processing for properties" a validated thermal model is required.

Microstructure The build microstructure can be related to the H13 phase diagram in Figure 2, although it must be noted that non-equilibrium conditions exist given the rapid heating and cooling rates. The microstructure shown was taken from the upper portion of a build, and for discussion has been separated into three different regions. Also shown is the height of the individual build passes. Region I is composed of as-solidified H13 (last pass) and supercritically reheated material. It can be seen that the last pass totally remelted the previous pass. Thermal cycles corresponding to these regions are also shown in the figure. Some segregation of alloying elements occurs as a result of partitioning during solidification, and little homogenization occurs due to the slow diffusion rates in austenite [Ref 5]. The exception is carbon for which the diffusivity is much more rapid and a uniform distribution is expected [Ref 5]. Microprobe measured segregation ratios (interdendritic boundaries)/(dendrite cores) were: Cr = 1.3, Mo = 1.2, and V= 1.5. The supercritical region extends from the liquidus temperature to the ferrite + carbide two-phase region, which on the equilibrium diagram is ~925°C. The light etching material of the supercritical region is untempered martensite in which no carbides were detected using transmission electron microscopy (TEM).

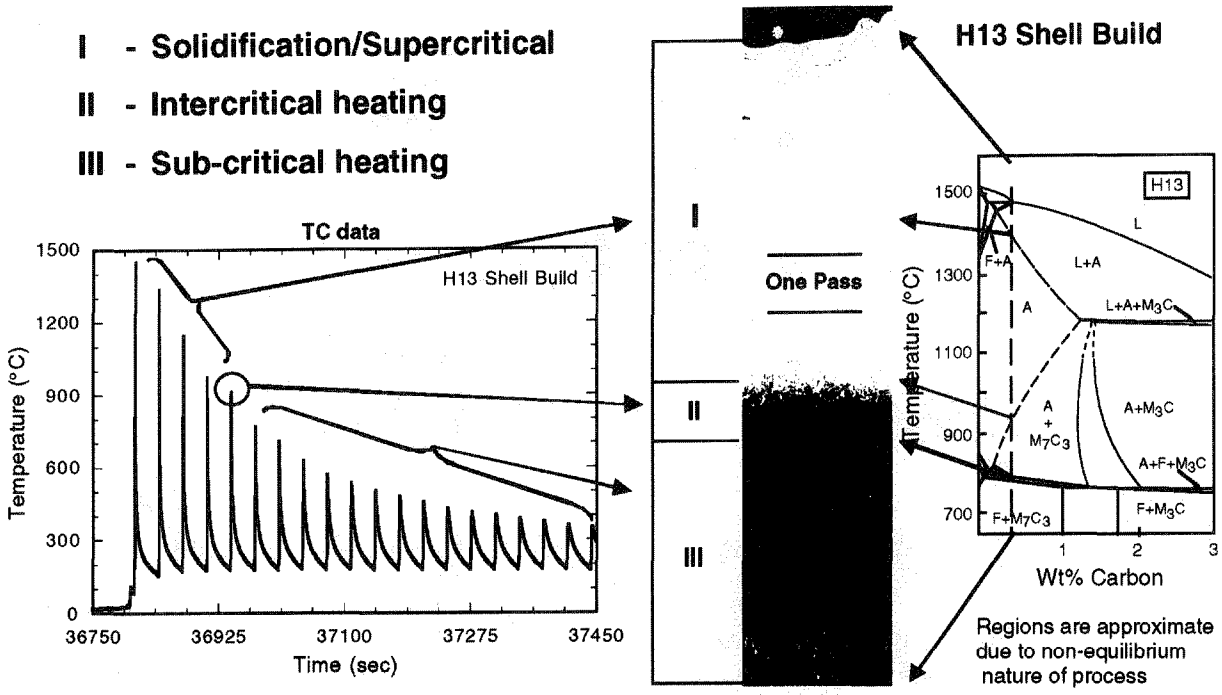

Figure 2 Correlation between measured thermal cycles, microstructure and the phase diagram used to describe H13 with 0.04 wt% C. Three thermal regions are used to describe the behavior. The pass height for these conditions is ≈0.25 mm.

Region II corresponds to material cycled into the intercritical two-phase and narrow three-phase regions shown on the diagram. This material had been previously cycled into the supercritical region, and corresponds to the first dark etching region noted in Figure 2. It is interesting that the height of this region is close to that of a single pass height, and based on the phase diagram, would have contained a thermal gradient of ~150°/0.25 mm (~600°C/mm). For the thermal cycles shown, only the peak temperature of the fifth thermal cycle lies within this region.

Region III contains the material that in addition to having experienced thermal cycles in the upper two regions, also experienced subcritical thermal cycles. The final microstructure consists of tempered martensite with a bimodal distribution of fine V (A areas) and larger Cr (B areas) containing carbides as shown in Figure 3.

H13 Aging Model A description of the overaging process in the H13 requires a numerical model that can be applied to the rapid thermal cycles associated with the LENS process. In this section a simple kinetic parameter is defined which relates hardness to thermal history. The model is based on classical coarsening models, and the additivity rule is used to apply the model to LENS thermal cycles. In the model development, a kinetic parameter that is simply related to hardness is defined first.

It is assumed that hardness is proportional to shear strength, and that the analysis for the strengthening effect of incoherent precipitates [Ref 7] applies,

$$H \propto \tau = \frac{\alpha \mu b}{\lambda} \qquad [1]$$

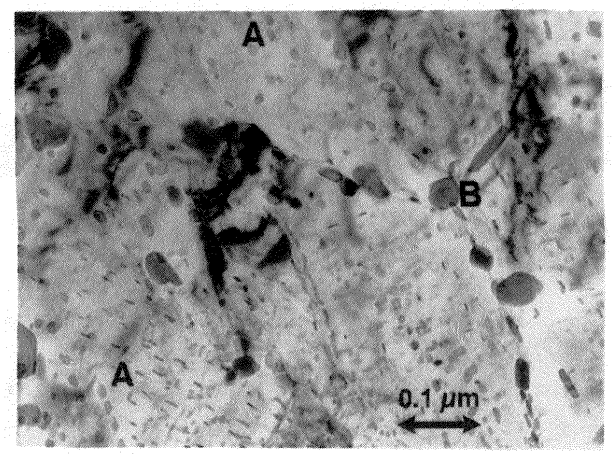

Figure 3 TEM image of H13 LENS deposit showing bimodal distribution of carbides. A and B denote typical regions of V and Cr rich carbides, respectively.

where H is the hardness, τ is the shear strength, α is a geometric factor, μ is the shear modulus, b is the burgers vector, and λ is the interparticle spacing. For overaging, the volume fraction of precipitates is assumed constant so that $\lambda \propto r$, where r is the radius of precipitates (assumed to be spherical). Thus, in the overaging regime, the following microstructural relationship is obtained:

$$H \propto \frac{1}{r}. \qquad [2]$$

During aging, the precipitates are assumed to follow classical coarsening kinetics [Ref 7] (*i.e.* Lifshitz and V. V. Slysov [Ref 8], and Wagner [Ref 9], or LSW kinetics), so that

$$\bar{r}_t^3 = \bar{r}_0^3 + Kt, \qquad [3]$$

where $\bar{r}_0$ is the mean initial particle radius and $\bar{r}_t$ is the particle radius at time t. The coefficient K in Equation 3 is generally given by an equation of the form

$$K = \frac{8}{9}\frac{D\sigma V_m C_\alpha(\infty)}{RT} f(\phi), \qquad [4]$$

where D is the diffusivity, σ is the interfacial energy, V_m is the molar volume of precipitate, $C_\alpha(\infty)$ is the solubility of the solute, R is the ideal gas constant, T is the temperature, and $f(\phi)$ is a function which depends on the particular coarsening theory ($f(\phi) = 1$ for the LSW theory). If it is assumed that all factors other than diffusivity are independent of temperature, and that the temperature dependence of D can be represented by $D = D_0\exp(-Q/RT)$, then Equation 4 can be written as

$$K = K_1 \frac{\exp\left(\frac{-Q}{RT}\right)}{T}, \qquad [5]$$

where K_1 is a constant. Combination of Equations 3 and 5 yields an expression for the coarsening rate as a function of time and temperature:

$$\bar{r}_t^3 = \bar{r}_0^3 + K_1 \frac{\exp\left(\frac{-Q}{RT}\right)}{T} t. \qquad [6]$$

Substitution of Equation 6 into Equation 2 (with $\bar{r}_t = r$) and rearranging leads to the result

$$H \propto K_2, \qquad [7]$$

where K_2 has the form

$$K_2 = \left(\bar{r}_0^3 + \frac{K_1 t \exp\left(\frac{-Q}{RT}\right)}{T} \right)^{-1/3} \qquad [8]$$

Thus, a plot of H versus K_2 should be linear. The most direct means to apply this methodology is to search for values of $\bar{r}_0$, K_1, and Q that maximize the linearity of the plot. This can easily be accomplished in a spreadsheet application. Alternatively, if values for any of the parameters are known, such as an initial size or the activation energy for the diffusion of the rate limiting precipitating species, these can be used to reduce the number of fit parameters.

Isothermal aging experiments were conducted on single-line LENS deposits to determine the model fit parameters. The hardness for different times and temperatures are shown in Figure 4(a). The results from the procedure described above to fit this data (Equations 7 and 8) are shown in Figure 4(b). The optimized fit parameters for this data set are $\bar{r}_0 = 3.99 \times 10^{-7}$, $K_1 = 0.04048$, and $Q/R = 38143$, and the hardness for any isothermal heat treatment can be represented by a line of the form

$$KHN = 285.31 + 1.495 \times 10^{-4}(K_2) \qquad r^2 = 0.9957. \qquad [9]$$

These parameters linearize the data over a wide range of aging conditions, including those conditions near peak hardening and overaged. The apparent activation energy for the softening, 75,790 cal/mole, is higher than might be expected for coarsening of alloy carbides in H13. For example, the activation energy for the diffusion of Mo in ferrite is given [Ref 10] as 57,700-60,000 cal/mole (the diffusion of Cr would be expected to have a similar activation energy). However, given the assumptions inherent in the model, such as spherical precipitates, etc., this discrepancy is not thought to be a major drawback with respect to the application of the model.

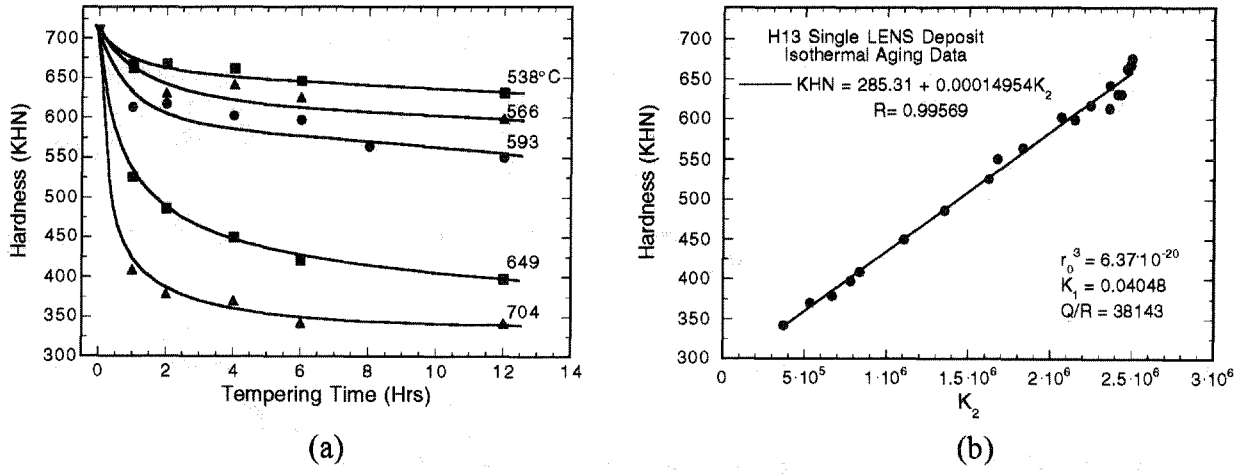

Figure 4 (a) Isothermal aging data for single line LENS deposits. (b) Correlation of data using Equations 7 and 8.

Application to LENS Thermal Cycles Application of the overaging model to LENS deposits requires a means to estimate the cumulative effect of the thermal cycle on the kinetics. A common approach for estimating this effect is the additivity principle [Ref 11, 12]. To apply the additivity principle, a thermal cycle is modeled as a series of small isothermal steps. At each step, the time elapsed is a fraction of the time required, at that temperature, to achieve a given amount of transformation or hardness. When these fractions sum to unity, the given hardness has been achieved. Formally, this can be written as

$$\int_0^t \frac{dt}{t_a(T)} = 1, \qquad [10]$$

where t is the time and $t_a(T)$ is the time to reach the given hardness isothermally. For discrete time steps, Equation 10 can be written in the summation form, or

$$\sum_0^t \frac{\Delta t}{t_a(T)} = 1. \qquad [11]$$

From Equation 9, $H = H_0 + mK_2$, where H_0 and m are the intercept and slope of the fit to the isothermal aging data, respectively, it is apparent that

$$H = H_0 + m\left(\bar{r}_0^3 + \frac{K_1 t \exp\left(\frac{-Q}{RT}\right)}{T}\right)^{-1/3} \qquad [12]$$

or, upon rearranging,

$$t = t_a(T) = \frac{T\left[\left(\frac{m}{H - H_o}\right)^3 - \bar{r}_0^3\right]}{K_1 \exp\left(\frac{-Q}{RT}\right)}. \qquad [13]$$

For an isothermal hold, Equation 13 represents the time required to reach a given hardness, H, at a given temperature, T. Using a series of small isothermal steps to represent a thermal cycle, the summation of Equation 11 can be solved by using a goal seeking routine to find the hardness that satisfies the summation for that thermal cycle. Alternatively, the summation can be solved sequentially by calculating the softening during a given time step, adjusting the temperature to the temperature associated with the next time step and adjusting the start time to that which it would have been had the temperature always been at the new temperature, and iterating this procedure over the entire thermal cycle.

Model Predictions vs. Experiment Microhardness tests conducted on wall builds showed that the hardness of the supercritical region was the same for all processing parameters, that of untempered martensite. The hardness dropped rapidly in the region of the first intercritical pass and then decreased little after subsequent build passes. It was also found that the highest hardness build corresponded to the lowest heat input deposit (200 watts and 9.3 mm/s) and the softest deposit corresponded to the highest heat input deposit (300 watts, 5.9 mm/s). This behavior is shown in Figure 5(a), where the hardness is plotted as a function of distance from the last pass for these two process conditions. The hardness changes are consistent with the model predictions shown in Figure 5(a). As a result of the rapid softening kinetics and its exponential

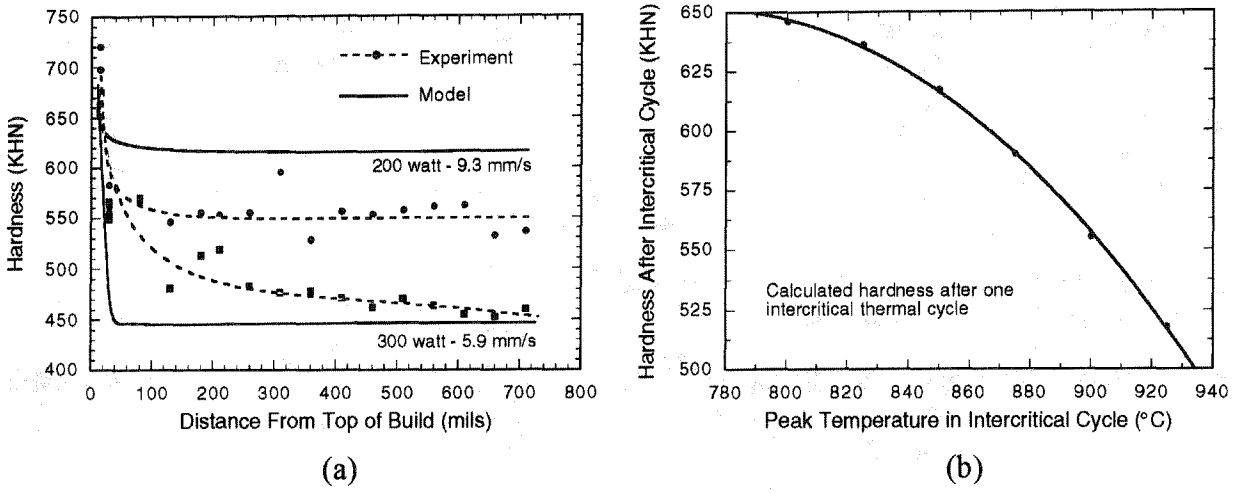

(a) (b)

Figure 5 (a) Comparison of measured and predicted hardness distributions in LENS H13 wall build. (b) Plot of calculated hardness as a function of peak temperature within the intercritical temperature range.

temperature dependence, the calculated hardness is primarily controlled by the peak temperature of the thermal cycle within the intercritical temperature region. The measured peak temperature of the high heat input build was higher than that of the lower heat input build which accounts for the predicted hardness differences for the two sets of parameters. Subsequent tempering passes are of similar duration as the first tempering pass, but at progressively lower temperature resulting in little additional tempering.

The model predictions in Figure 5(b) show that hardness strongly depends on the peak temperature of the single thermal cycle within the intercritical region. For a region that experiences a peak temperature of 800°C, the hardness drops from ~710 KHN (that of untempered martensite) to ~645 KHN. For a peak temperature of 925°C, the hardness drops to ~515 KHN. The tempering response, or predicted hardness is, however, much more complex. It must be remembered that a thermal gradient is associated with the peak temperature of each tempering pass. All the temperatures within the intercritical and upper subcritical regions will correspond to the peak temperatures at some specific point, or line along the build. Furthermore, the height of the passes are on the order of the intercritical zone of the first tempering pass. Thus one would expect that a hardness gradient should exist over individual passes. Also, there could be regions further down the build that would be harder than regions closer to the top. This was actually observed, and accounts for some of the scatter in the data shown in Figure 5(a) and the banded etching behavior of the microstructure, Figure 2. To average some of the localized variation, Each hardness value plotted in Figure 5(a) is actually the average of three measurements made along a line at the same distance from the top of the build.

The temperature cycles used in the calculations were those experimentally measured with thermocouples. Although these thermocouples are small (0.13 mm diameter), they are still one half the height of the individual build passes. As shown in the microstructure of Figure 2, in the intercritical region the thermocouples lie within a temperature gradient of ~600°C/mm and therefore provide some average temperature within the temperature gradient. Nevertheless, the peak temperatures measured with the thermocouples resulted in the correct trend of calculated hardness for the builds, Figure 5(a). This is likely a result of the thermal gradient being flatter in the high power low speed build than in the low power high speed build, rather than the thermal couple placement. In general it was found that the hardness correlates better with travel speed than with laser power [Ref 13]. Thus, it can be seen that the details of the hardness and

tempering kinetics are highly dependent upon the height of the individual build passes as well as the thermal gradient in the intercritical region of the first tempering pass. Furthermore, accurate predictions of hardness require precise knowledge of the local thermal history.

Summary and Conclusions

The potential to use LENS to process for properties was demonstrated using H13 tool steel. The development and integration of both process and material models is necessary for precise property control. A simple kinetic model was developed that related thermal history to hardness for H13 and was combined with LENS thermal data to estimate build hardness. A good correlation was obtained between the nature of the predicted and measured hardness of single line thickness wall builds, although the features of intercritical heating require further investigation to achieve a more representative description. It was shown that the steep thermal gradients and rapid softening kinetics in H13 require very precise knowledge of the thermal history to accurately predict properties. With the rapid carbide coarsening kinetics of H13, almost all of the softening occurred during the first thermal cycle within the tempering regime.

Acknowledgements

The support of Mike Oliver in LENS processing and the metallurgical support of Annette Newman, both of Sandia Laboratories are greatly appreciated. This work was funded by the United States Department of Energy under Contract # DE-AC04-94AL85000.

References

1. M. L. Griffith, D. M. Keicher, C. L. Atwood, J. A. Romero, J. E. Smugeresky, L. D. Harwell, and D. L. Greene, *Proceedings of the Solid Freeform Fabrication Symposium*, Austin TX, , (1996), pp. 125-131.
2. D. Rosenthal, *Trans ASME*, Nov (1946), pp. 849-866.
3. J. Dike, C. Cadden, R. Corderman, C. Schultz and M. McAninch, *Trends in Welding Research, Proc. 4th International Conference*, Eds. Smart, Johnson and David, ASM, (1996), pp. 57-65.
4. J. J. Dike, J. A. Brooks, J. S. Krafcik, *Trends in Welding Research, Proc. 4th International Conference*, Eds. Smart, Johnson and David, ASM, (1996), pp.159-164.
5. J. A. Brooks, M. I. Baskes, and F. A. Greulick, *Metall. Trans. A*, 22A, (1991), pp. 915-925.
6. J. N. Dupont, C. V. Robino, and A. R. Marder, *Acta Materiallia*, Vol. 46, (1998), pp. 4781-4790.
7. R. E. Smallman, *Modern Physical Metallurgy, - Fourth Edition*, Butterworths, London, (1985), pp. 394-407.
8. I. M. Lifshitz and V. V. Slyozov, *J. Phys. Chem. Solids*, Vol. 19, (1961), pp. 35-50.
9. C. Wagner, Z. Elektrochem., Vol. 65, (1961), pp. 581-591.
10. E. A. Brandes, *Smithells Metals Reference Book Sixth Edition*, Butterworths, London, (1983), p. 13–64.
11. E. Scheil, *Archiv. fur Eisenhuttenwesen*, Vol. 12, (1935), pp. 565-567.
12. J. W. Christian, *The Theory of Phase Transformations in Metals and Alloys Part I*, Pergamon Press, New York, (1981), pp. 542-548.
13. M. Griffith, E. Schlinger, L. Harwell, M. Oliver, M. Baldwin, M. Ensz, J. Brooks, C. Robino, J. Smugeresky, W. Hofmeister, M. Wert, and D. Nelson, *Materials and Design*, Vol. 20, Elsevier Science Ltd, (1999), pp. 107-213.